

Aromatic and antiaromatic ring currents in a molecular nanoring

Martin D. Peeks¹, Timothy D. W. Claridge¹ & Harry L. Anderson¹

Aromatic and antiaromatic molecules—which have delocalized circuits of $[4n + 2]$ or $[4n]$ electrons, respectively—exhibit ring currents around their perimeters^{1–4}. The direction of the ring current in an aromatic molecule is such as to generate a magnetic field that opposes the external field inside the ring (a ‘diatropic’ current), while the ring current in an antiaromatic molecule flows in the reverse direction (‘paratropic’)⁵. Similar persistent currents occur in metal or semiconductor rings, when the phase coherence of the electronic wavefunction is preserved around the ring^{6,7}. Persistent currents in non-molecular rings switch direction as a function of the magnetic flux passing through the ring, so that they can be changed from diatropic (‘aromatic’) to paratropic (‘antiaromatic’) simply by changing the external magnetic field. As in molecular systems, the direction of the persistent current also depends on the number of electrons⁸. The relationship between ring currents in molecular and non-molecular rings is poorly understood, partly because they are studied in different size regimes: the largest aromatic molecules have diameters of about one nanometre, whereas persistent currents are observed in microfabricated rings with diameters of 20–1,000 nanometres. Understanding the connection between aromaticity and quantum-coherence effects in mesoscopic rings provides a motivation for investigating ring currents in molecules of an intermediate size⁹. Here we show, using nuclear magnetic resonance spectroscopy and density functional theory, that a six-porphyrin nanoring template complex, with a diameter of 2.4 nanometres, is antiaromatic in its 4+ oxidation state (80 π electrons) and aromatic in its 6+ oxidation state (78 π electrons). The antiaromatic state has a huge paramagnetic susceptibility, despite having no unpaired electrons. This work demonstrates that a global ring current can be promoted in a macrocycle by adjusting its oxidation state to suppress the local ring currents of its components. The discovery of ring currents around a molecule with a circumference of 7.5 nanometres, at room temperature, shows that quantum coherence can persist in surprisingly large molecular frameworks.

Studies on annulenes have led to the conclusion that aromaticity decreases with increasing ring size and vanishes for systems with more than about 30 π electrons (corresponding to a diameter of around 1.3 nm)^{10,11}, but it seems likely that aromaticity can be preserved in larger systems if geometrical disorder is suppressed¹². The previous record for the largest aromatic molecule is held by a 50 π dodecaphyrin with a diameter of about 1.3 nm (ref. 13). The dication of [8]cycloparaphenylene (30 π , diameter 1.1 nm) is also aromatic¹⁴. We recently reported the synthesis of π -conjugated macrocycles consisting of 5–50 porphyrin units, with diameters of 2–20 nm, (*c*-PN, $N = 5–50$, Fig. 1), as well as the corresponding linear oligomers *l*-PN^{15–17}. The *c*-PN rings might all be expected to exhibit diatropic or paratropic ring currents around the whole nanoring because they all have circumferential circuits of $[4n + 2]$ or $[4n]$ π electrons (for example, *c*-P6 84 π ; *c*-P7 98 π), yet, as in [8]cycloparaphenylene, the neutral molecules exhibit no signs of global aromaticity or antiaromaticity.

Density functional theory (DFT) calculations of the nucleus-independent chemical shift (NICS)¹⁸ at the centre of the ring (Supplementary Table 2) provide insights into the behaviour of the *c*-P6 nanoring cations, indicating aromaticity for the 6+ oxidation state, while 0 (neutral) and 12+ are non-aromatic, and 4+ is antiaromatic. The NICS(0)_{iso} calculated on a grid in the *x*–*y* plane (the plane of the six Zn atoms) for *c*-P6, *c*-P6⁴⁺, *c*-P6⁶⁺ and *c*-P6¹²⁺ clearly demonstrates the nature of the ring current in each oxidation state (Fig. 2 and Supplementary Fig. 8). For the neutral *c*-P6, the shielding effects are localized above and below the plane of each porphyrin unit, with no net global ring current (Fig. 2a). This result is in stark contrast to *c*-P6⁴⁺, where the NICS is positive (nuclear magnetic resonance (NMR) deshielding) inside the macrocycle, and negative (shielding) outside, characteristic of paratropicity (Fig. 2b). This effect is reversed in the aromatic *c*-P6⁶⁺, with shielding inside the macrocycle, and deshielding outside (Fig. 2c). The NICS(0)_{iso} grid for the 12+ oxidation state (Supplementary Fig. 8) shows local porphyrin antiaromaticity, with no global aromaticity, consistent with six local 16 π antiaromatic porphyrin ring currents. For the 6+ oxidation state, we also calculated NICS_{zz} in the orthogonal *x*–*z* and *y*–*z* planes (Supplementary Figs 6 and 7), showing that the shielding anisotropy of the nanoring extends as a double cone above and below the plane of the ring. Models of the anisotropy of the induced current density (ACID)¹⁹ support the conclusions from NICS, demonstrating a coherent current ACID isosurface for *c*-P6⁴⁺ and *c*-P6⁶⁺ (with paratropic and diatropic current directions, respectively; current vectors shown in Supplementary Fig. 9), in contrast to an interrupted isosurface for *c*-P6 and *c*-P6¹²⁺ (Fig. 2d–f and Supplementary Fig. 9). Many antiaromatic systems, including cyclobutadiene, undergo a Jahn–Teller distortion to favour a low-symmetry conformation and this effect is evident in *c*-P6⁴⁺. The geometries of *c*-P6 and *c*-P6⁶⁺ converge in *D*_{6h} symmetry, whereas *c*-P6⁴⁺ has *C*₁ symmetry with an elliptical flattening factor of $f = 0.049$ (defined as $1 - b/a$, where *a* and *b* are the major and minor radii of the 6-Zn ellipse). *c*-P6¹²⁺ also has *C*₁ symmetry but in this case there is almost no ellipticity ($f < 10^{-3}$).

The nanoring cations can be generated in solution by chemical or electrochemical oxidation. Square-wave voltammetry of *c*-P6·T6 reveals six reversible porphyrin-centred oxidations in a first manifold, at +0.1 V to +0.7 V (versus Fc/Fc⁺, where Fc is ferrocene) (Fig. 3; see Supplementary Fig. 13 for spectroelectrochemistry). The second manifold comprises a single six-electron oxidation to generate *c*-P6·T6¹²⁺, in which each porphyrin unit is in its 2+ oxidation state. All of the oxidation states are accessible by titration with tris(2,4-dibromophenyl)aminium hexafluoroantimonate (DIBAHA_F, $E_{\text{red}} = 1.14$ V), and specific oxidation states can be targeted with diacetylferrocenium hexafluoroantimonate ($E_{\text{red}} = 0.50$ V), tris(4-bromophenyl)aminium hexafluoroantimonate (BAHA_F, $E_{\text{red}} = 0.70$ V) and thianthrenium hexafluoroantimonate (Thn, $E_{\text{red}} = 0.86$ V) (all versus Fc/Fc⁺, Fig. 3, Supplementary Fig. 1 for structures)²⁰. The magnetic effects of molecular ring currents are particularly apparent in NMR spectra^{1–5}. Titration of DIBAHA_F into a solution of *c*-P6·T6

¹University of Oxford, Department of Chemistry, Chemistry Research Laboratory, Oxford OX1 3TA, UK.

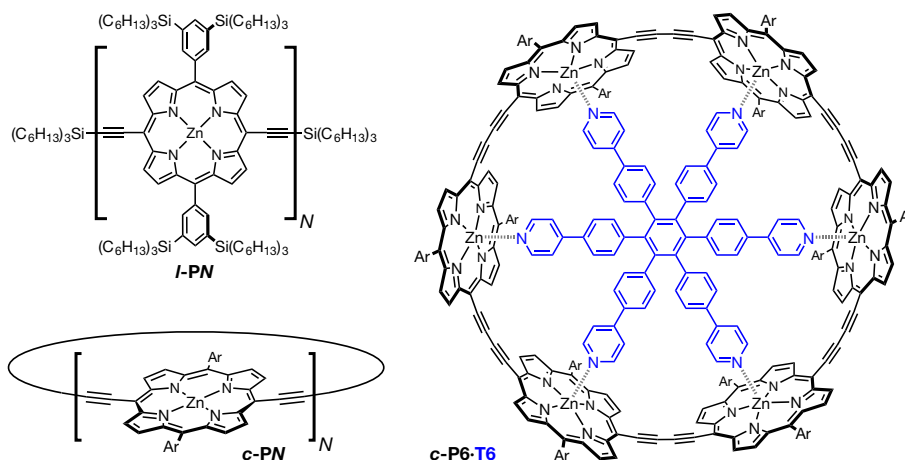


Figure 1 | Molecular structures of the butadiyne-linked porphyrin oligomers used in this study. *L*-PN, *c*-PN and *c*-P6·T6. Ar = (3,5-bis(triethylsilyl))phenyl as shown for *L*-PN.

at 223 K in CD_2Cl_2 gives a sequence of three resolved ^1H NMR spectra (Fig. 4), assigned to the 4+ (red-brown solution), 6+ (burgundy solution) and 12+ (grey/black solution) oxidation states (see below). There is no further change in the NMR spectrum upon addition of excess DIBAHF: the 12+ oxidation state is the endpoint. Identical spectra are obtained using $\text{AgSbF}_6/\text{I}_2$ (4:1 or 2:1) as the oxidant. Intermediates with odd numbers of electrons are not observed during these titrations, presumably because their spectra are extremely broad. The spectrum for the 2+ oxidation state (that is, after addition of 2 equivalents of oxidant) is also too broad to observe, indicating that $\text{c-P6}\cdot\text{T6}^{2+}$ is open-shell and paramagnetic. We confirmed the oxidation state of the first two resolved products (4+ and 6+) by single-point oxidations with diacetylferrocenium (4+), BAHA_F (6+) and Thn (6+). These single-point oxidation NMR spectra are reproducible in the presence or absence of supporting electrolyte (0.1 M Bu_4NPF_6).

Before presenting the NMR evidence for global nanoring (anti)aromaticity in the 4+ and 6+ oxidation states, we calibrate discussion of the ^1H NMR spectra on the well studied²¹ neutral $\text{c-P6}\cdot\text{T6}$. The porphyrin β -pyrrole protons resonate at the characteristic chemical shifts for neutral porphyrins (*a*: 9.56 parts per million (p.p.m.), *b*: 8.75 p.p.m.,

Fig. 4a; Supplementary Table 3). Rotation of *meso*-aryl groups is slow on the NMR timescale (see Methods for details), so that the outer and inner *ortho* protons (*o* and *o'*) and trihexylsilyl resonances (THS and THS') can be confidently distinguished. A global aromatic ring current would shield the inner protons (*o'* and THS') and deshield the outer protons (*o* and THS), causing large differences in chemical shift ($\Delta\delta = \delta_{\text{inner}} - \delta_{\text{outer}}$). It is observed that these signals give small chemical shift differences ($\Delta\delta_{o'/o} = 0.26$ p.p.m.; $\Delta\delta_{\text{THS'}/\text{THS}} = 0.14$ p.p.m., for the terminal CH_3 group) in the neutral ring, implying that there is no global ring current. The ring current of each aromatic 18π porphyrin unit is apparent from the ^1H chemical shifts of the template protons α , β , γ and δ , which are shielded by the porphyrin; the shielding is attenuated with increasing distance from the porphyrin: $\alpha \gg \beta > \gamma > \delta$ (Fig. 4a and Supplementary Table 4).

The ^1H NMR spectrum of $\text{c-P6}\cdot\text{T6}^{4+}$ is very broad (Fig. 4b), precluding detailed assignment of the resonances. However, a clear splitting of the THS groups is apparent in the aliphatic region (Supplementary Fig. 22). The less shielded set of THS resonances shows multiple nuclear Overhauser effects on resonances at high chemical shift ($\delta = 8\text{--}24$ p.p.m.), and is thus assigned to the inner THS' group

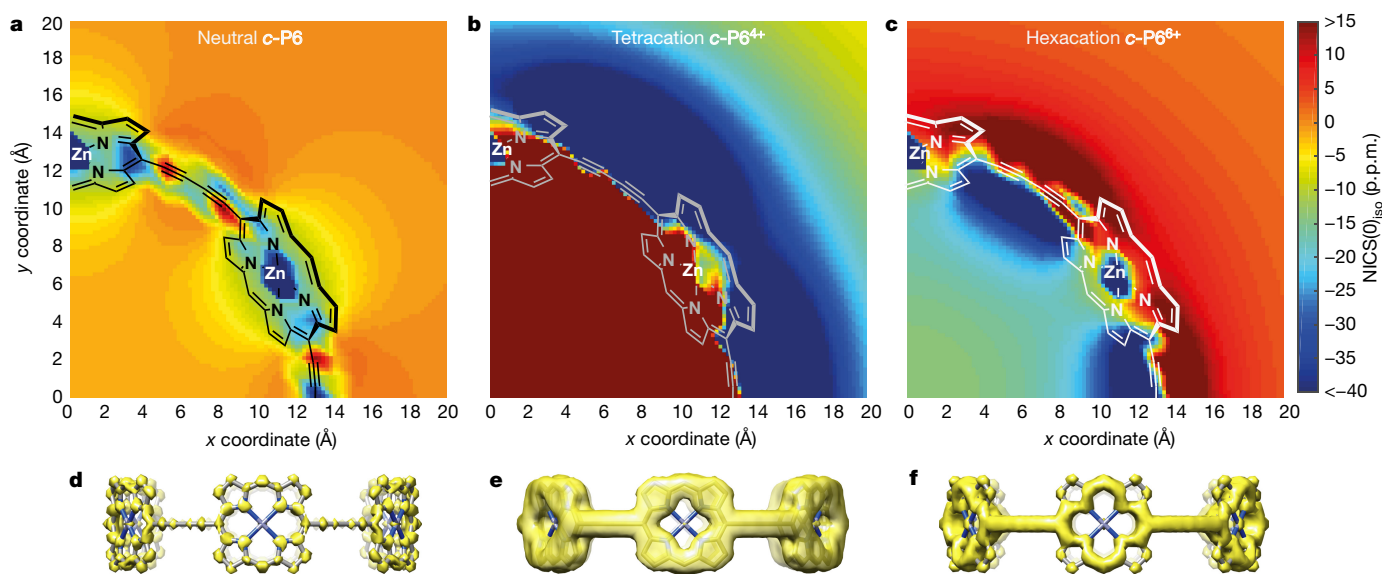


Figure 2 | Computational data supporting aromaticity and antiaromaticity. a–c, NICS(0)_{iso} grids in the *x*–*y* plane of *c*-P6 (a), *c*-P6⁴⁺ (b) and *c*-P6⁶⁺ (c). The colour axis is truncated to compare the grids on the same scale; see Supplementary Fig. 8 for grids with individual scales. d–f, ACID plots for each oxidation state. The yellow iso-surface depicts the

anisotropy of the induced current density (isovalue 0.1 a.u.). The neutral oxidation state (a, d) shows ring current effects local to each porphyrin subunit. In contrast, the 4+ and 6+ oxidation states (b, e and c, f) show global ring currents, manifest by sign-reversal of the NICS inside/outside the ring.

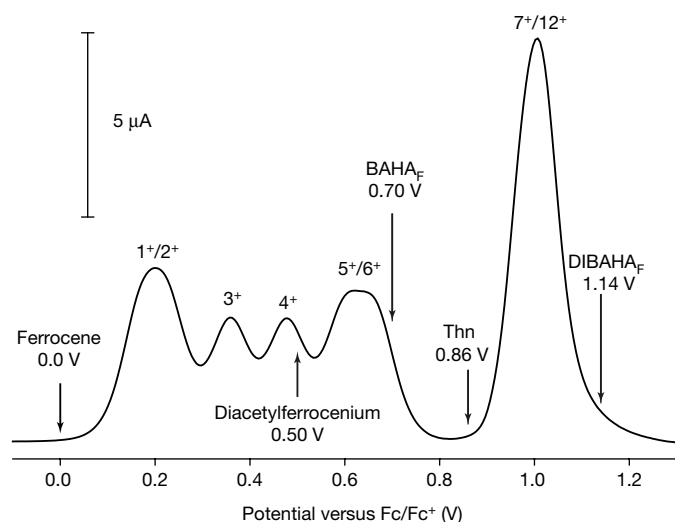


Figure 3 | Square-wave voltammetry of *c*-P6-T6. The solvent was CH_2Cl_2 (0.1 M Bu_4NPF_6). The arrows show the first reduction potential of each oxidant²⁰: ferrocene, diacetylferrocenium, tris(4-bromophenyl)aminium hexafluoroantimonate (BAHA_F), thianthrenium hexafluoroantimonate (Thn) and tris(2,4-dibromophenyl)aminium hexafluoroantimonate (DIBAHA_F). There are six oxidations in a first manifold, generating oxidation states up to the hexacation ($6+$). A second manifold contains only a single oxidation wave generating the dodecacation ($12+$).

(Supplementary Fig. 19). The large positive $\Delta\delta_{\text{THS}'/\text{THS}}$ (3.45 p.p.m.) implies a strong macrocyclic paratropic ring current. Antiaromaticity is further supported by an extremely high paramagnetic susceptibility exaltation for *c*-P6-T6⁴⁺ measured by Evans' NMR method²² and corroborated by DFT calculations. The molar magnetic susceptibility χ_{mol} (experimental) = 21,000 p.p.m. $\text{cm}^3 \text{mol}^{-1}$, the effective magnetic moment $\mu_{\text{eff}} = 6.5 \mu_{\text{B}}$, χ_{mol} (calculated) = 68,000 p.p.m. $\text{cm}^3 \text{mol}^{-1}$, and $\mu_{\text{eff}} = 11.5 \mu_{\text{B}}$, compared to the values of $\chi_{\text{mol}} = 1,480$ p.p.m. $\text{cm}^3 \text{mol}^{-1}$ and $\mu_{\text{eff}} = 1.7 \mu_{\text{B}}$ expected for a single unpaired electron (μ_{B} is the Bohr magneton and all units are cgs; see Supplementary Fig. 4 and Supplementary Table 2). Despite many predictions of paramagnetism in closed-shell antiaromatic compounds²³, to the best of our knowledge, this is the first time that the effect has been observed experimentally, though diamagnetic susceptibility exaltation is a well recognized characteristic of aromatic systems²⁴. Experimental studies of other antiaromatic systems have found a reduction in the diamagnetism rather than outright paramagnetism²⁴. 'Giant orbital paramagnetism' has been predicted, but not observed, for carbon-based nanostructures such as carbon nanotube tori²⁵.

In contrast to *c*-P6-T6⁴⁺, the NMR spectrum of *c*-P6-T6⁶⁺ is well resolved and fully assigned by two-dimensional techniques (see Supplementary Figs 20, 23 and 24). A large $\Delta\delta$ is observed between the o'/o (−1.87 p.p.m.) and THS'/THS (−0.70 p.p.m.) resonances. Nuclear Overhauser effects on the template were used to assign the inner versus outer resonances. The inner o' and THS' are more shielded than their external counterparts (negative $\Delta\delta$) in *c*-P6-T6⁶⁺, confirming the presence of a global diatropic ring current. The template protons α – δ are all nearly equally shielded with respect to unbound T6 (Supplementary Table 4), revealing a uniform shielding effect within the macrocycle, as predicted by the NICS grids (Fig. 2c), and indicating the absence of local porphyrin aromaticity.

The ^1H NMR spectrum of *c*-P6-T6¹²⁺ is well resolved and was fully characterized by two-dimensional NMR techniques (Supplementary Figs 21, 25 and 26). In *c*-P6-T6¹²⁺, every porphyrin unit is in the antiaromatic 16π dicationic oxidation state²⁶. The antiaromatic porphyrin centres deshield the template protons (with respect to unbound template, Supplementary Table 4); the extent of deshielding decreases with distance from the porphyrin plane, $\alpha \gg \beta > \gamma > \delta$ (Fig. 4d). This

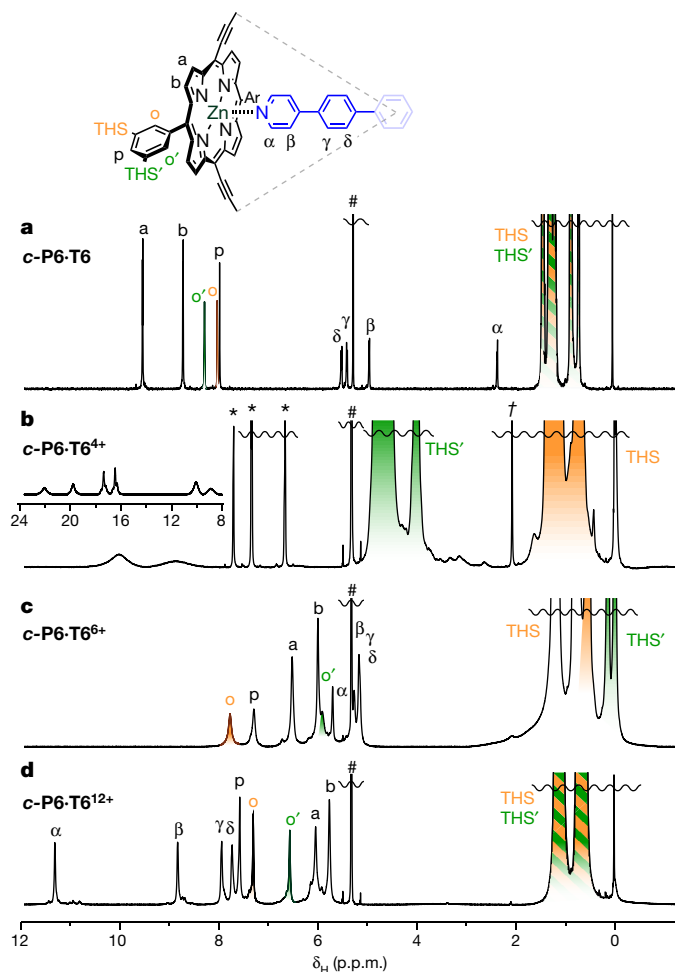


Figure 4 | NMR spectra of neutral and oxidised *c*-P6-T6. a–d, ^1H NMR (500 MHz, CD_2Cl_2) of neutral *c*-P6-T6 at 298 K (a); *c*-P6-T6⁴⁺ generated by titration with DIBAHA_F at 223 K (b); *c*-P6-T6⁶⁺ generated by titration with $\text{AgSbF}_6/\text{I}_2$ at 223 K (c); and *c*-P6-T6¹²⁺ generated by oxidation with excess DIBAHA_F at 223 K (d). The inset shows the molecular structure of the repeat unit of the sixfold symmetric *c*-P6-T6. The peaks labelled # and * arise from CH_2Cl_2 and neutral oxidant (tris(2,4-dibromophenyl)amine), respectively. Unlabelled resonances are not assigned. † is an unidentified impurity. In the neutral state (a), the template resonances (α – δ) probe the local aromaticity of each porphyrin. This aromaticity is reversed in the dodecacation (d), where the template protons report local antiaromaticity. The global aromaticity and antiaromaticity of the tetracation (b) and hexacation (c) are revealed by the large chemical shift difference between similar protons inside and outside the ring. The full spectra, without truncated peaks, are shown in Supplementary Fig. 27.

behaviour is entirely local to the 16π porphyrin unit, as demonstrated by the similarity between the ^1H NMR spectra of the porphyrin monomer *I*-P1²⁺, dimer *I*-P2⁴⁺, tetramer *I*-P4⁸⁺, and cyclic oligomers *c*-P6-T6¹²⁺, *c*-P6-T6¹²⁺, *c*-P8-T8¹⁶⁺, *c*-P10-T10²⁰⁺, *c*-P11-T11²²⁺ and *c*-P12-T12²⁴⁺ (all recorded in the presence of excess DIBAHA_F ; Supplementary Figs 10 and 11). Comparison of the square-wave voltammetry of *I*-P1 and *I*-P2 shows that the first oxidation wave of *I*-P1 is split upon oligomer homologation, while the second oxidation wave is not split (Supplementary Fig. 12). This lack of electronic communication is reflected in the highest occupied molecular orbital (HOMO) of *I*-P2⁴⁺, corresponding to the Gouterman a_{1u} orbital²⁷, which exhibits no density at the porphyrin *meso* positions (Supplementary Fig. 14). In contrast, the HOMOs of neutral oligomers exhibit high density at the *meso* positions (Gouterman a_{2u}), leading to strong electronic communication in *meso*–*meso* linked porphyrin oligomers²⁸.

The ^1H NMR spectra of c-P6^{6+} and c-P6^{12+} with no bound template are very similar to those of the template complexes, except for the absence of template signals (Supplementary Figs 15 and 16). We were unable to observe a ^1H NMR spectrum of c-P6^{4+} without the bound template, and the conformational lock provided by the template seems to be essential for creating a well defined antiaromatic system. Neutral butadiyne-linked porphyrin oligomers (with no bound template) have a very low barrier to torsional rotation about the alkyne axis²⁹ and fast exchange occurs between the *ortho* (*o* and *o'*) resonances in c-P6 , even at low temperature, owing to this free rotation. In contrast, the *o* and *o'* resonances are split at low temperature for c-P6^{6+} ($T < 263\text{ K}$; Supplementary Fig. 17) and c-P6^{12+} ($T < 243\text{ K}$; Supplementary Fig. 18), indicating increased conjugation between porphyrin subunits in these oxidation states. Exchange spectroscopy (EXSY)³⁰ NMR experiments at 213 K revealed ΔG^\ddagger of $49.5 \pm 0.4\text{ kJ mol}^{-1}$ and $42.6 \pm 0.4\text{ kJ mol}^{-1}$ for the 6+ and 12+ oxidation states, respectively (see Methods, Supplementary Figs 2 and 3, and Supplementary Table 1 for details). The c-P6^{6+} hexacation is aromatic with or without the bound T6 template, but the template has two important roles in this system: it holds the nanoring in a regular geometry, resulting in sharper NMR spectra, and it provides a set of protons to probe the magnetic effects of the ring current at well defined positions inside the nanoring.

Online Content Methods, along with any additional Extended Data display items and Source Data, are available in the online version of the paper; references unique to these sections appear only in the online paper.

Received 26 July; accepted 8 November 2016.

Published online 19 December 2016.

- Spitler, E. L., Johnson, C. A., II & Haley, M. M. Renaissance of annulene chemistry. *Chem. Rev.* **106**, 5344–5386 (2006).
- Krygowski, T. M., Cyrański, M. K., Czarnocki, Z., Häfeli, G. & Katritzky, A. R. Aromaticity: a theoretical concept of immense practical importance. *Tetrahedron* **56**, 1783–1796 (2000).
- Gleiter, R. & Haberhauer, G. *Aromaticity and Other Conjugation Effects* (Wiley-VCH, 2012).
- Lazzeretti, P. Ring currents. *Prog. NMR Spectrosc.* **36**, 1–88 (2000).
- Gomes, J. A. N. F. & Mallion, R. B. Aromaticity and ring currents. *Chem. Rev.* **101**, 1349–1384 (2001).
- Bleszynski-Jayich, A. C. *et al.* Persistent currents in normal metal rings. *Science* **326**, 272–275 (2009).
- Lorke, A. *et al.* Spectroscopy of nanoscopic semiconductor rings. *Phys. Rev. Lett.* **84**, 2223–2226 (2000).
- Loss, D. & Goldbart, P. Period and amplitude halving in mesoscopic rings with spin. *Phys. Rev. B* **43**, 13762–13765 (1991).
- Mayor, M. & Didschies, C. A giant conjugated molecular ring. *Angew. Chem. Int. Ed.* **42**, 3176–3179 (2003).
- Wannere, C. S. & von Ragué Schleyer, P. How aromatic are large $(4n + 2)\pi$ annulenes? *Org. Lett.* **5**, 865–868 (2003).
- Choi, C. H. & Kertesz, M. Bond length alternation and aromaticity in large annulenes. *J. Chem. Phys.* **108**, 6681–6688 (1998).
- Soncini, A., Fowler, P. W. & Jenneskens, L. W. Ring currents in large $[4n + 2]$ -annulenes. *Phys. Chem. Chem. Phys.* **6**, 277–284 (2004).
- Soya, T., Kim, W., Kim, D. & Osuka, A. Stable [48]-, [50]-, and [52]dodecaphyrins (1.1.0.1.1.0.1.1.0.1.1.0): the largest Hückel aromatic molecules. *Chem. Eur. J.* **21**, 8341–8346 (2015).
- Toriumi, N., Muranaka, A., Kayahara, E., Yamago, S. & Uchiyama, M. In-plane aromaticity in cycloparaphenylene dications: a magnetic circular dichroism and theoretical study. *J. Am. Chem. Soc.* **137**, 82–85 (2015).

- Kondratuk, D. V. *et al.* Supramolecular nesting of cyclic polymers. *Nat. Chem.* **7**, 317–322 (2015).
- Liu, P. *et al.* Synthesis of five-porphyrin nanorings by using ferrocene and corannulene templates. *Angew. Chem. Int. Ed.* **55**, 8358–8362 (2016).
- Sprafke, J. K. *et al.* Belt-shaped π -systems: relating geometry to electronic structure in a six-porphyrin nanoring. *J. Am. Chem. Soc.* **133**, 17262–17273 (2011).
- Chen, Z., Wannere, C. S., Corminboeuf, C., Puchta, R. & von Ragué Schleyer, P. Nucleus-independent chemical shifts (NICS) as an aromaticity criterion. *Chem. Rev.* **105**, 3842–3888 (2005).
- Geuenich, D., Hess, K., Kohler, F. & Herges, R. Anisotropy of the induced current density (ACID), a general method to quantify and visualize electronic delocalization. *Chem. Rev.* **105**, 3758–3772 (2005).
- Connelly, N. G. & Geiger, W. E. Chemical redox agents for organometallic chemistry. *Chem. Rev.* **96**, 877–910 (1996).
- Karunanithy, G. *et al.* Harnessing NMR relaxation interference effects to characterise supramolecular assemblies. *Chem. Commun. (Camb.)* **52**, 7450–7453 (2016).
- Evans, D. F. 400. The determination of the paramagnetic susceptibility of substances in solution by nuclear magnetic resonance. *J. Chem. Soc.* 2003–2005 (1959).
- Tellgren, E. I., Helgaker, T. & Soncini, A. Non-perturbative magnetic phenomena in closed-shell paramagnetic molecules. *Phys. Chem. Chem. Phys.* **11**, 5489–5498 (2009).
- Dauben, H. J. Jr, Wilson, J. D. & Laity, J. L. Diamagnetic susceptibility exaltation in hydrocarbons. *J. Am. Chem. Soc.* **91**, 1991–1998 (1969).
- Tamura, R., Ikuta, M., Hirahara, T. & Tsukada, M. Positive magnetic susceptibility in polygonal nanotube tori. *Phys. Rev. B* **71**, 045418 (2005).
- Yamamoto, Y. *et al.* Synthesis, reactions, and electronic properties of 16 π -electron octaisobutyltetraphenylporphyrin. *J. Am. Chem. Soc.* **132**, 12627–12638 (2010).
- Gouterman, M. Spectra of porphyrins. *J. Mol. Spectrosc.* **6**, 138–163 (1961).
- Lin, V. S.-Y. & Therien, M. J. The role of porphyrin-to-porphyrin linkage topology in the extensive modulation of the absorptive and emissive properties of a series of ethynyl- and butadiynyl- bridged bis- and tris(porphinato)zinc chromophores. *Chem. Eur. J.* **1**, 645–651 (1995).
- Peeks, M. D., Neuhaus, P. & Anderson, H. L. Experimental and computational evaluation of the barrier to torsional rotation in a butadiyne-linked porphyrin dimer. *Phys. Chem. Chem. Phys.* **18**, 5264–5274 (2016).
- Perrin, C. L. & Dwyer, T. J. Application of two-dimensional NMR to kinetics of chemical exchange. *Chem. Rev.* **90**, 935–967 (1990).

Supplementary Information is available in the online version of the paper.

Acknowledgements We thank the ERC (grant 320969), the EPSRC and the John Templeton Foundation for support, B. Odell for help with NMR spectroscopy and the Oxford Advanced Research Computing (ARC) centre for the high-performance computing provision (<http://dx.doi.org/10.5281/zenodo.22558>). M.D.P. thanks Exeter College, Oxford, for further support.

Author Contributions M.D.P. synthesized the compounds, performed the calculations, collected and analysed the spectroscopic data. T.D.W.C. assisted with NMR data collection and interpretation. H.L.A. devised the project. M.D.P. and H.L.A. wrote the paper. All authors discussed the results and edited the manuscript.

Author Information Reprints and permissions information is available at www.nature.com/reprints. The authors declare no competing financial interests. Readers are welcome to comment on the online version of the paper. Correspondence and requests for materials should be addressed to H.L.A. (harry.anderson@chem.ox.ac.uk).

Reviewer Information *Nature* thanks M. Bröring and the other anonymous reviewer(s) for their contribution to the peer review of this work.

METHODS

Note on terminology. A 'diatropic current' indicates an aromatic system, and a 'paratropic current' an antiaromatic system. The terms 'diatropic' and 'paratropic' relate to the direction of the induced ring current around the conjugated aromatic system, as described in the main text.

Experimental method. All porphyrin compounds were synthesized as described previously³¹. Bulky 3,5-bis(trihexylsilyl)phenyl solubilising sidegroups were chosen to permit high-concentration NMR experiments, and to inhibit aggregation. **c-P6-T6** was synthesized from 200 mg of monomer **I-P1** and small amounts of larger rings (**c-P8** to **c-P16**) were isolated as side products, characterized by gel permeation chromatography, NMR, MALDI-TOF mass spectrometry and ultraviolet-vis-near-infrared optical spectroscopy.

Oxidation experiments used the hexafluoroantimonate salts of diacylferrocenium $E_{\text{red}} = 0.50$ V versus Fc/Fc⁺, tris(4-bromophenyl)aminium (BAHA_{BF}, $E_{\text{red}} = 0.70$ V versus Fc/Fc⁺), thianthrenium (Thn, $E_{\text{red}} = 0.86$ V versus Fc/Fc⁺) and tris(2,4-dibromophenyl)aminium (DIBAHA_{BF}, $E_{\text{red}} = 1.14$ V versus Fc/Fc⁺), and also silver hexafluoroantimonate with iodine ($E_{\text{red}} > 1.14$ V versus Fc/Fc⁺) (Supplementary Fig. 1)²⁰. All oxidation experiments were conducted in J. Young tap NMR tubes using CD₂Cl₂ stored over molecular sieves, using standard Schlenk line techniques. For titrations, a solution of oxidant (40–50 mM) was added to a solution of porphyrin compound (about 4 mg ml^{−1}) in the NMR tube, cooled to −78 °C and kept under a flow of argon. For single point oxidations, an excess of an oxidant as a solution or suspension was added to the porphyrin solution in the same manner. Tubes were then closed and quickly transferred to an NMR spectrometer pre-cooled to the appropriate temperature. Exposure to water is immediately deleterious to porphyrin polycations, but they are stable to oxygen (O₂). The use of rubber septa (Subaseal) was avoided: we found that the introduction of small quantities of rubber (even by non-coring needles) has an immediate quenching effect on the cations. NMR measurements were performed on a Bruker AVII 500 (5 mm TXI probe) or a Bruker AVIII 700 (5 mm TCI cryoprobe). Chemical shifts are reported in parts per million versus the residual solvent peak. The ¹H NMR spectra of **c-P6-T6**⁴⁺ and **c-P6-T6**⁶⁺ are unchanged on warming from 213 K to 278 K. In contrast, the spectrum of **c-P6-T6**¹²⁺ broadens upon warming, and this change becomes irreversible if the sample is kept at 20 °C for more than a few minutes, owing to decomposition. Neutral **c-P6-T6** is insoluble in CD₂Cl₂ at low temperatures (<233 K), but solubility improves upon oxidation. The ¹H NMR spectra of all species are field-independent, from 500 MHz (11.7 T) to 700 MHz (16.4 T). The reversibility of oxidations was confirmed by NMR spectra collected after reduction, with ferrocene, of cation samples.

Voltammetric measurements were made using an Autolab PGSTAT 12 with a glassy-carbon working electrode, platinum wire counter electrode and Ag/AgCl quasi-reference electrode. Voltammograms were referenced to the Fc/Fc⁺ couple (0.0 V) as an internal reference after each measurement. Square wave voltammograms were acquired with a 5-mV step potential, 50-mV modulation amplitude and 5-Hz frequency. Exclusion of water was essential for the acquisition of clean voltammograms. The supporting electrolyte salt (tetra-*n*-butylammonium hexafluorophosphate, Bu₄NPF₆, TBAP) was dried by melting under vacuum. CH₂Cl₂ (dried over alumina (MBraun SPS), distilled from CaH₂, and stored over 4-Å molecular sieves) was added to the dry electrolyte to a concentration of 0.1 M electrolyte. Analyte solutions were prepared by addition of this electrolyte solution to porphyrin oligomer (2–10 mg), and measurements were performed over 4-Å molecular sieves.

Spectroelectrochemistry measurements used an optically transparent thin layer electrochemical (OTTLE) cell comprising a three-electrode system sandwiched between two CaF₂ optical windows, with a path length of approximately 200 μm. The working and auxiliary electrodes were platinum gauzes, and the quasi-reference electrode was a silver wire. Near-infrared spectra were recorded using a Bruker Vertex 80, and IR spectra using a Bruker Tensor 27. Cyclic voltammograms were measured using a Palmsens EmStat3+ with scan rates of 10 mV s^{−1} and 5 mV s^{−1} for the near-infrared and infrared measurements, respectively.

Details of computational chemistry methods. DFT calculations were all performed using a model of **c-P6** in which solubilizing aryl groups had been removed (*D*_{6h} initial symmetry). Geometries were optimized using Gaussian09/D.01³² and the B3LYP/6-31G* functional/basis set combination^{33–35}. The neutral and 6+ rings converged to *D*_{6h} symmetry, while the 4+ and 12+ rings lost symmetry (*C*₁). The 2+ ring was optimized with both unrestricted and restricted DFT, and the stability of triplet and singlet wavefunctions were checked in the former case. The 2+ oxidation state optimized to *C*_{2h} symmetry and a singlet ground state with spin contamination (*S*²) = 0.7342 (0.2022 after annihilation). The converged geometry optimised structures were confirmed as minima by performing frequency calculations, which showed no imaginary frequencies. NICS/susceptibility and ACID calculations were conducted using the GIAO and CSGT methods, respectively, as implemented in Gaussian09/D.01. NICS grids were calculated with 1 Å

resolution on a 20 Å × 20 Å grid. Version 2.0 of the ACID program¹⁹ (external to Gaussian) was used to generate the ACID results, and they were visualized using POV-Ray. Application of Grimme's D3 dispersion correction³⁶ to geometry optimizations did not affect the conclusions of subsequent NICS calculations. The D3 correction caused small changes in the geometries (root-mean-square deviation 0.018–0.025 Å) and this affected the NICS by 0%–5% of their B3LYP values. The M06-2X and ωB97X-D functionals^{37,38} were tested on the 0+, 4+, 6+ and 12+ oxidation states and gave similar NICS values to B3LYP (Supplementary Table 5). M06-2X is a highly parameterized hybrid meta GGA (generalized gradient approximation) functional with good performance for main group thermochemistry and non-covalent interactions. ωB97X-D is a long-range corrected hybrid GGA functional with an empirical dispersion correction term, and similar areas of applicability as M06-2X with the addition of good treatment of the self-interaction error. The magnitude of NICS(0) for the antiaromatic 4+ oxidation state decreases according to B3LYP > M06-2X > ωB97X-D owing to a corresponding increase in ellipticity (*f* = 0.049, 0.088 and 0.166 for B3LYP, M06-2X and ωB97X-D, respectively). For ωB97X-D, this elliptical distortion results in predicted non-aromaticity of the 4+ state. The presence of template (**T6**) in the experimental studies maintains an approximately circular geometry by limiting such distortion, assuring antiaromaticity.

Processing software. NMR spectra were processed using TopSpin version 3.0. EXSY data were fitted using the Curve Fitting Tool in MATLAB and errors were propagated with the help of the Python (3.5) uncertainties package. Figures were composed in Adobe Illustrator and Inkscape. Spectroelectrochemical and NICS surface plots were generated using MATLAB. Molecular orbitals were visualized using Chimera.

The interporphyrin torsion barriers in c-P6⁶⁺ and c-P6¹²⁺. In template-free neutral **c-P6**, the barrier to inter-porphyrin torsion about the butadiene linkers is likely to be similar to that in **I-P2**, about 2.1 kJ mol^{−1} (ref. 29), so the porphyrins are rapidly rotating at room temperature (*k*_B*T* = 2.5 kJ mol^{−1}). Consequently, only one resonance is observed in ¹H NMR for the *o* and *o'* (ortho) protons in fast exchange. No broadening is apparent when reducing temperature to 223 K in CD₂Cl₂, below which solubility becomes limiting. In contrast, the *o/o'* resonances in oxidized nanorings **c-P6**⁶⁺ and **c-P6**¹²⁺ are in slow exchange at 223 K.

Variable temperature NMR can be used to determine the coalescence temperature *T*_c between the *o* and *o'* resonances and hence the exchange activation barrier at *T*_c (via the Eyring equation). Estimates of *T*_c from variable temperature NMR are >278 K and ~233 K for 6+ and 12+, respectively. Estimation of *T*_c is confounded by broadening of the entire spectrum of oxidized species at elevated temperatures, perhaps owing to paramagnetic exchange with residual oxidant. To avoid this problem, we used two-dimensional EXSY NMR to measure the exchange rate constant *k* at 213 K for **c-P6**⁶⁺ and **c-P6**¹²⁺.

A phase-sensitive NOESY (nuclear Overhauser effect spectroscopy, which in this context is two-dimensional exchange spectroscopy, EXSY) pulse sequence with gradient enhancement (noesygpph) was employed with variable mixing times *t*_{mix} from 5 ms to 125 ms. The recycle delay (*d*₁) was 1 s. The Fourier-transformed (with a squared sine bell window function applied to the measured free induction decay) spectra were phase-corrected and a two-dimensional baseline of fifth order was subtracted. The intensities of peaks of interest were determined by volume integration.

The pertinent *o/o'* exchange was modelled as a simple two-spin system, with spins labelled *A* and *B*. An equal population of sites *A* and *B* was assumed, leading to the following equalities for the intensities *I* of on-diagonal peaks (*I*_{AA} and *I*_{BB}) and off-diagonal crosspeaks (*I*_{AB} and *I*_{BA})^{30,39}. These equalities are not experimental facts, owing to spectral overlap, but this does not affect the analysis.

$$I_{AA} = I_{BB} \text{ and } I_{AB} = I_{BA}$$

The intensities *I* can be defined as follows:

$$I_{AA} = \frac{1}{4} e^{-\frac{t_{\text{mix}}}{T_1}} (1 + e^{-kt_{\text{mix}}}) M^0$$

and

$$I_{AB} = \frac{1}{4} e^{-\frac{t_{\text{mix}}}{T_1}} (1 - e^{-kt_{\text{mix}}}) M^0$$

where *t*_{mix} is exchange mixing time, *T*₁ is the relaxation time constant (assumed equal for *A* and *B*), *k* is the exchange rate constant and *M*⁰ is the initial magnetization. If we take the ratio of intensities *r*, the equations simplify, removing the dependencies on *M*⁰ and *T*₁:

$$r = \frac{I_{AB} + I_{BA}}{I_{AA} + I_{BB}}$$

$$r = \frac{1 - e^{-kt_{\text{mix}}}}{1 + e^{-kt_{\text{mix}}}}$$

The experimental data points and fit for 6+ and 12+ are shown in Supplementary Figs 2 and 3, respectively.

The equations for I_{AA} and I_{AB} are based on the following chemical system:



which, given the equal populations of A and B, leads to the following definition of k (ref. 39), for $p_{\text{A}} = p_{\text{B}} = 0.5$:

$$k_{\text{AB}} = p_{\text{B}}k$$

$$k_{\text{BA}} = p_{\text{A}}k$$

$$k = 2k_{\text{AB}} = 2k_{\text{BA}} = k_{\text{AB}} + k_{\text{BA}}$$

In 1992, Green *et al.*⁴⁰ noted that a multiplicative factor of two must be applied to k_{obs} ($=k_{\text{AB}}$) determined by magnetization transfer experiments for equally populated two-site exchange in order to deliver a k_{chem} suitable for the calculation of ΔG^\ddagger . The rationale is that a species at the midpoint of a symmetric reaction profile will only decay in such a way that gives rise to magnetization transfer 50% of the time. This notion is the direct analogue of the transmission coefficient κ in the Eyring equation:

$$k = \kappa \frac{k_{\text{B}}T}{h} e^{-\frac{\Delta G^\ddagger}{RT}}$$

In words, if we denote labelling with an asterisk, the species A^*B will form a transition state in which the label is no longer well-defined: $[AB]^*$. This transition state can decay with 50% probability (owing to the symmetric nature of the reaction profile) to give A^*B and AB^* . A rate constant k_{AB} describes only those transition states which result in magnetization transfer from A to B, so a value of $\kappa = 0.5$ must be used, analogous to Green's multiplicative factor of two for k_{chem} (that is, $k_{\text{chem}} = 2k_{\text{obs}} = k_{\text{AB}}/\kappa$). In our case the formulations of k , I_{AA} and I_{AB} give us k_{chem} directly³⁹, such that we use a transmission coefficient of $\kappa = 1$ to determine ΔG^\ddagger . The results are shown in Supplementary Table 1: $k_{213\text{ K}}$ is about 3 s^{-1} and 172 s^{-1} for 6+ and 12+, respectively.

The chemical exchange rate constant at the coalescence temperature (T_c) can be determined by taking an estimate for $\Delta\nu$ between o/o' in slow exchange from the templated nanoring spectra (Supplementary Tables 2 and 3), and thus T_c can be estimated using ΔG^\ddagger from the above analysis. The quantitative analysis of errors in this EXSY experiment is difficult—rather than relying on the 95% confidence interval of the fit (0.07 s^{-1} and 35 s^{-1} for 6+ and 12+, respectively), we have adopted an empirical error of 25%.

On the basis of the absence of exchange broadening in neutral **c-P6** at 223 K (hence $T_c \ll 223\text{ K}$, and $k_{\text{ex}} = 578\text{ s}^{-1}$ at T_c), an upper bound of $\Delta G^\ddagger \ll 42.3\text{ kJ mol}^{-1}$ can be assigned for the neutral oxidation state. The value of the exchange rate constant k at 213 K for **c-P6**⁶⁺ is of the same order as that measured for o/o' exchange due to aryl rotation about the *meso*-aryl bond in a similar complex (a templated [10]-porphyrin nanoring), at 298 K: 4 s^{-1} and 0.4 s^{-1} for two inequivalent porphyrin sites⁴¹. These values of k correspond to ΔG^\ddagger of 70 kJ mol^{-1} and 263 kJ mol^{-1} , respectively, and are thus unlikely to contribute to the EXSY spectra at 213 K. Furthermore, no o/o' exchange is observed in the 223 K EXSY spectra of **c-P6-T6**⁶⁺ and **c-P6-T6**¹²⁺ with $t_{\text{mix}} = 250\text{ ms}$.

Paramagnetic susceptibility by Evans' method. We applied the principles of Evans' method^{22,42–44} for the determination of magnetic susceptibility by NMR to determine the approximate magnetic susceptibilities of the [6]-porphyrin nanoring oxidation states. At the outset, we expected to observe increases in paramagnetic susceptibility for the odd oxidation states (1+, 3+, 5+) and for the free oxidant, with near-zero relative magnetic susceptibility for the closed-shell oxidation states.

The Evans' method involves separating an analyte and a reference solution by placing one in an isolated coaxial chamber within the other. In our case, we placed a flame-sealed capillary of CFCl_3 in d_8 -toluene into a standard 5-mm J. Young NMR tube containing the analyte solution, CFCl_3 and CD_2Cl_2 . The reference capillary was supported with custom-made poly(tetrafluoroethylene) (PTFE) spacers. With this assembly, we were able to conduct titrations of oxidant into **c-P6-T6** solutions, and measure the frequency shift between the CFCl_3 resonances in the ^{19}F domain. We chose to use CFCl_3 since the ^1H domain was too crowded to permit reliable measurement of a chemical shift difference between analyte and reference probe resonances for the commonly used references. However, the ^{19}F resonance for

CFCl_3 is split into a complicated multiplet pattern owing to different isotopic chemical shift effects from $^{35/37}\text{Cl}$ (the resonance resembles the mass spectrum isotope pattern for CFCl_3 , Supplementary Fig. 4b). For this reason, we use d_8 -toluene as the solvent in our reference capillary, to provide an appreciable initial frequency difference $\Delta\nu$ between analyte and reference chamber CFCl_3 resonances, and make subsequent measurements of $\Delta\nu$ (calculated relative to the $\Delta\nu$ between CFCl_3 resonances in the reference and analyte compartments in otherwise pure solvent without **c-P6-T6**) more reliable.

Attempts to use Evans' method without an explicit reference compound, instead monitoring the ^2H solvent resonances, failed owing to the broad linewidth and low signal-to-noise ratio of the ^2H spectrum. Control experiments indicated that, in the absence of analyte, $\Delta\nu$ with CFCl_3 varied by about 1 Hz per kelvin of temperature variation. In the context of a titration, this implies an error of at least $\pm 2\text{ Hz}$ in each $\Delta\nu$.

A titration of DIBAHAF (about 44.5 mM, in 21 μl increments) into **c-P6-T6** (about 2.0 mM, 450 μl in CD_2Cl_2) was conducted at 243 K. At this concentration and field, one equivalent of oxidant (2.0 mM, that is, $2.0 \times 10^{-6}\text{ mol cm}^{-3}$) with a magnetic moment of $1\mu_{\text{B}}$ would give an imperceptible (1–2 Hz) frequency difference $\Delta\nu$. However, our experimental results (Supplementary Fig. 4) show a huge $\Delta\nu$ (66 Hz) for the antiaromatic tetracation **c-P6-T6**⁴⁺. This surprising result corresponds to a large paramagnetic susceptibility and is supported by DFT calculations for **c-P6** (Supplementary Fig. 4 and Supplementary Table 2).

The magnetic susceptibility χ_{mol} is related to the chemical shift difference $\Delta\nu$ by:

$$\chi_{\text{mol}} = -\frac{3\Delta\nu}{4\pi\nu_0c}$$

Where ν_0 is the spectrometer frequency (470 MHz) and c is the concentration of **c-P6**, in moles per cubic centimetre. A diamagnetic solvent correction has been neglected from this analysis.

Data availability. The computational (Cartesian coordinates and NICS and ACID results) and experimental (NMR spectra) data that support the findings of this study are available in the Oxford University Research Archive with the identifier doi:10.5287/bodleian:JVB5KZaD0 (ref. 45). Other data are available upon reasonable request to H.L.A.

- Tait, C. E., Neuhaus, P., Peeks, M. D., Anderson, H. L. & Timmel, C. R. Transient EPR reveals triplet state delocalization in a series of cyclic and linear π -conjugated porphyrin oligomers. *J. Am. Chem. Soc.* **137**, 8284–8293 (2015).
- Frisch, M. J. *et al.* *Gaussian 09 Revision D.01* (Gaussian Inc. 2009).
- Becke, A. D. Density-functional thermochemistry. III. The role of exact exchange. *J. Chem. Phys.* **98**, 5648–5652 (1993).
- Hehre, W. J., Ditchfield, R. & Pople, J. A. Self-consistent molecular orbital methods. XII. Further extensions of Gaussian-type basis sets for use in molecular orbital studies of organic molecules. *J. Chem. Phys.* **56**, 2257–2261 (1972).
- Rassolov, V. A., Pople, J. A., Ratner, M. A. & Windus, T. L. 6-31G* basis set for atoms K through Zn. *J. Chem. Phys.* **109**, 1223–1229 (1998).
- Grimme, S., Antony, J., Ehrlich, S. & Krieg, H. A consistent and accurate ab initio parameterization of density functional dispersion correction (DFT-D) for the 94 elements H-Pu. *J. Chem. Phys.* **132**, 154104 (2010).
- Zhao, Y. & Truhlar, D. G. The M06 suite of density functionals for main group thermochemistry, thermochemical kinetics, noncovalent interactions, excited states and transition elements: two new functionals and systematic testing of four M06-class functionals and 12 other functionals. *Theor. Chem. Acc.* **120**, 215–241 (2008).
- Chai, J.-D. & Head-Gordon, M. Long-range corrected hybrid density functionals with damped atom-atom dispersion corrections. *Phys. Chem. Chem. Phys.* **10**, 6615–6620 (2008).
- Jeener, J., Meier, B. H., Bachmann, P. & Ernst, R. R. Investigation of exchange processes by two-dimensional NMR spectroscopy. *J. Chem. Phys.* **71**, 4546–4549 (1979).
- Green, M. L. H., Wong, L. L. & Sella, A. Relationship between intramolecular chemical exchange and NMR-observed rate constants. *Organometallics* **11**, 2660–2668 (1992).
- Liu, S. *et al.* Caterpillar track complexes in template-directed synthesis and correlated molecular motion. *Angew. Chem. Int. Ed.* **54**, 5355–5359 (2015).
- Schubert, E. M. Utilizing the Evans method with a superconducting NMR spectrometer in the undergraduate laboratory. *J. Chem. Educ.* **69**, 62 (1992).
- Grant, D. H. Paramagnetic susceptibility by NMR. *J. Chem. Educ.* **72**, 39–40 (1995).
- Piguet, C. Paramagnetic susceptibility by NMR: the “solvent correction” removed for large paramagnetic molecules. *J. Chem. Educ.* **74**, 815–816 (1997).
- Peeks, M. D., Claridge, T. D. W. & Anderson, H. L. Data for ‘aromatic and antiaromatic ring currents in a molecular nanoring’. <http://dx.doi.org/10.5287/bodleian:JVB5KZaD0> (Oxford University Research Archive, 2016).